DTU Library

NuSTAR unveils a compton-thick 2 quasar in MrK 34

Gandhi, P.; Lansbury, G. B.; Alexander, D. M.; Stern, D.; Arevalo, P.; Ballantyne, D. R.; Balokovic, M.; Bauer, F. E.; Boggs, S. E.; Brandt, W. N.

NuSTAR UNVEILS A COMPTON-THICK TYPE 2 QUASAR IN MrK 34

P. Gandhi[1], G. B. Lansbury[1], D. M. Alexander[1], D. Stern[2], P. Arévalo[3,4], D. R. Ballantyne[5], M. Baloković[6],
F. E. Bauer[3,7,8], S. E. Boggs[9], W. N. Brandt[10,11], M. Brightman[12], F. E. Christensen[13], A. Comastri[14],
W. W. Craig[13,15], A. Del Moro[1], M. Elvis[16], A. C. Fabian[17], C. J. Hailey[18], F. A. Harrison[6],
R. C. Hickox[19], M. Koss[20], S. M. LaMassa[21], B. Luo[9,10], G. M. Madejski[22], A. F. Ptak[23],
S. Puccetti[24,25], S. H. Teng[26], C. M. Urry[21], D. J. Walton[6], and W. W. Zhang[23]
[1] Department of Physics, Durham University, South Road, Durham DH1 3LE, UK
[2] Jet Propulsion Laboratory, California Institute of Technology, 4800 Oak Grove Drive, Mail Stop 169-221, Pasadena, CA 91109, USA
[3] Instituto de Astrofísica, Facultad de Física, Pontificia Universidad Catolica de Chile, Casilla 306, Santiago 22, Chile
[4] Instituto de Física y Astronomía, Facultad de Ciencias, Universidad de Valparaíso, Gran Bretana N 1111, Playa Ancha, Valparaíso, Chile
[5] Center for Relativistic Astrophysics, School of Physics, Georgia Institute of Technology, Atlanta, GA 30332, USA
[6] Cahill Center for Astrophysics, California Institute of Technology, 1216 East California, Boulevard, Pasadena, CA 91125, USA
[7] Millennium Institute of Astrophysics
[8] Space Science Institute, 4750 Walnut Street, Suite 205, Boulder, CO 80301, USA
[9] Space Sciences Laboratory, University of California, Berkeley, CA 94720, USA
[10] Department of Astronomy and Astrophysics, The Pennsylvania State University, 525 Davey Lab, University Park, PA 16802, USA
[11] Institute for Gravitation and the Cosmos, The Pennsylvania State University, University Park, PA 16802, USA
[12] Max-Planck-Institut für extraterrestrische Physik, Giessenbachstrasse 1, D-85748 Garching bei München, Germany
[13] DTU Space-National Space Institute, Technical University of Denmark, Elektrovej 327, DK-2800 Lyngby, Denmark
[14] INAF Osservatorio Astronomico di Bologna, via Ranzani 1, I-40127 Bologna, Italy
[15] Lawrence Livermore National Laboratory, Livermore, CA 94550, USA
[16] Harvard-Smithsonian Center for Astrophysics, 60 Garden Street, Cambridge, MA 02138, USA
[17] Institute of Astronomy, Madingley Road, Cambridge CB3 0HA, UK
[18] Columbia Astrophysics Laboratory, Columbia University, 550 W 120th Street, NY 10027, USA
[19] Department of Physics and Astronomy, Dartmouth College, 6127 Wilder Laboratory, Hanover, NH 03755, USA
[20] Institute for Astronomy, Department of Physics, ETH Zurich, Wolfgang-Pauli-Strasse 27, CH-8093 Zurich, Switzerland
[21] Yale Center for Astronomy and Astrophysics, Physics Department, Yale University, P.O. Box 208120, New Haven, CT 06520-8120, USA
[22] Kavli Institute for Particle Astrophysics and Cosmology, Stanford University, 2575 Sand Hill Road M/S 29, Menlo Park, CA 94025, USA
[23] X-Ray Astrophysics Laboratory, NASA Goddard Space Flight Center, Greenbelt, MD 20771, USA
[24] ASDC-ASI, Via del Politecnico, I-00133 Roma, Italy
[25] INAF-Osservatorio Astronomico di Roma, via Frascati 33, I-00040 Monte Porzio Catone (RM), Italy
[26] Observational Cosmology Laboratory, NASA Goddard Space Flight Center, Greenbelt, MD 20771, USA
Received 2014 April 22; accepted 2014 July 6; published 2014 August 22

ABSTRACT

We present *Nuclear Spectroscopic Telescope Array* (*NuSTAR*) 3–40 keV observations of the optically selected Type 2 quasar (QSO2) SDSS J1034+6001 or Mrk 34. The high-quality hard X-ray spectrum and archival *XMM-Newton* data can be fitted self-consistently with a reflection-dominated continuum and a strong Fe Kα fluorescence line with equivalent width >1 keV. Prior X-ray spectral fitting below 10 keV showed the source to be consistent with being obscured by Compton-thin column densities of gas along the line of sight, despite evidence for much higher columns from multiwavelength data. *NuSTAR* now enables a direct measurement of this column and shows that $N_{\rm H}$ lies in the Compton-thick (CT) regime. The new data also show a high intrinsic 2–10 keV luminosity of $L_{2-10} \sim 10^{44}$ erg s^{-1}, in contrast to previous low-energy X-ray measurements where $L_{2-10} \lesssim 10^{43}$ erg s^{-1} (i.e., X-ray selection below 10 keV does not pick up this source as an intrinsically luminous obscured quasar). Both the obscuring column and the intrinsic power are about an order of magnitude (or more) larger than inferred from pre-*NuSTAR* X-ray spectral fitting. Mrk 34 is thus a "gold standard" CT QSO2 and is the nearest non-merging system in this class, in contrast to the other local CT quasar NGC 6240, which is currently undergoing a major merger coupled with strong star formation. For typical X-ray bolometric correction factors, the accretion luminosity of Mrk 34 is high enough to potentially power the total infrared luminosity. X-ray spectral fitting also shows that thermal emission related to star formation is unlikely to drive the observed bright soft component below ∼3 keV, favoring photoionization instead.

Key words: galaxies: active – X-rays: galaxies – X-rays: individual (Mrk 34)

Online-only material: color figures

1. INTRODUCTION

The census of active galactic nuclei (AGNs) remains severely incomplete at high gas column densities ($N_{\rm H}$). The line-of-sight column $N_{\rm H}$(los) becomes optically thick to Thomson scattering above $\approx 1.2 \times 10^{24}$ cm^{-2} for typical cosmic abundances. This is the Compton-thick or "CT" regime. CT sources provide a significant contribution to the cosmic X-ray background (CXB) spectrum, with most CXB models requiring a CT AGN contribution of around 10%–25% to the CXB peak flux at ≈30 keV (e.g., Comastri et al. 1995; Gandhi & Fabian 2003; Gilli et al. 2007; Treister et al. 2009; Draper & Ballantyne 2010; Akylas et al. 2012; Ueda et al. 2014). However, only ≈20 bona fide CT Seyferts have been confirmed in the local universe, where $N_{\rm H}$(los) can be robustly measured from self-consistent spectral fitting based upon a significant hard X-ray continuum (>10 keV) and detection of a strong neutral Fe Kα line with equivalent width (EW) $\gtrsim$ 1 keV (Della Ceca et al. 2008;

Goulding et al. 2012). These features result from the suppression of direct photons, leading to a dominant contribution from reflection off circumnuclear gas.

The number density of obscured AGNs is even more uncertain at higher luminosities. "Type 2 quasars" (QSO2s) are characterized by luminous narrow emission lines in the optical/infrared and the absence of broad lines, as would be expected if significant circumnuclear obscuration is present. The radio-loud subset of these, or powerful "radio galaxies," were the first to be identified (e.g., McCarthy 1993; Miley & De Breuck 2008), and X-ray studies have shown many of them to be heavily obscured along the line of sight (e.g., Gandhi et al. 2006; Tozzi et al. 2009; Wilkes et al. 2013). Now, the dominant population of radio-quiet QSO2s is being revealed through homogeneous, wide-area selection through both mid-infrared color selection from *Spitzer* and *WISE* (e.g., Lacy et al. 2004; Stern et al. 2005, 2012; Donley et al. 2012; Mateos et al. 2012; Assef et al. 2013) and spectroscopic identification by the Sloan Digital Sky Survey (SDSS; e.g., Zakamska et al. 2003; Reyes et al. 2008).

Sloan-selected QSO2s, or SDSS-QSO2s, are identified as sources with $L_{[O\,III]} \gtrsim 10^{8.3} L_\odot$ for the forbidden [O III] $\lambda 5007$ line and an absence of broad permitted lines, but selection is also based upon redshift-dependent line flux ratios, which are required for removing star-forming galaxies as well as a spectroscopic signal-to-noise selection. X-ray follow-up has shown most SDSS-QSO2s to be consistent with the unified AGN scheme in having significant columns of obscuring gas (Vignali et al. 2004, 2006; Ptak et al. 2006; Jia et al. 2013). By using known mid-infrared to X-ray and [O III] to X-ray luminosity relations, Vignali et al. (2010) infer that about half of SDSS-QSO2s are obscured by CT gas columns. This is an important conclusion but is, at present, an *indirect* one, because it is based upon many X-ray non-detections and assumptions of the intrinsic AGN spectral shapes. There is a known degeneracy between the strength of reflection and obscuring column density (Gandhi et al. 2007; Treister et al. 2009) that can only be resolved using high-quality hard X-ray data (e.g., Matt et al. 2000; Ricci et al. 2011; Vasudevan et al. 2013; Del Moro et al. 2014).

X-ray surveys can potentially address these issues by selecting optically faint and radio-quiet obscured quasars with $L_{2-10\,keV} \gtrsim 10^{44}$ erg s^{-1} and $N_H > 10^{22}$ cm^{-2} (e.g., Gandhi et al. 2004; Mainieri et al. 2011; Merloni et al. 2014). However, confirmation of CT X-ray obscuration in distant quasars requires the very deepest pencil-beam surveys, and few sources have enough counts for detailed spectral characterization (Norman et al. 2002; Stern et al. 2002; Feruglio et al. 2011; Comastri et al. 2011; Brightman & Ueda 2012; Georgantopoulos et al. 2013). The study of distant quasars ($z \gtrsim 2$) is aided by the redshifting of hard X-ray photons to the energy range below 10 keV where most sensitive X-ray observatories have operated thus far. This is not the case for low redshift quasars, leaving significant uncertainties in the modeling of their X-ray spectra even though they appear brighter.

As a result of all these issues, the contribution of QSO2 activity to the CXB, as well as to AGN growth and evolution, remain uncertain. However, the latest synthesis models predict that obscured quasars outnumber unobscured ones at high redshift ($z \sim 2$) where the peak of black hole and galaxy growth occur (Ueda et al. 2014). An accurate census of QSO2s is thus clearly important.

The *Nuclear Spectroscopic Telescope Array* (*NuSTAR*; Harrison et al. 2013) is the first mission in orbit capable of true imaging at energies of $\sim$3–79 keV with an angular reso-

lution better than previous hard X-ray observatories by over an order of magnitude. This enables an effective gain of $\gtrsim 100$ for direct studies of the broadband hard X-ray continua of a variety of cosmic sources. The CXB peak at ≈ 30 keV lies within *NuSTAR*'s operational energy range, and we expect to resolve $\sim$30% of its integrated flux (Ballantyne et al. 2011), as compared to the current $\sim$1% level (Burlon et al. 2011; Vasudevan et al. 2013). We may also expect to better elucidate the QSO2 contribution to the overall AGN population. In a first look at the hard X-ray sky with *NuSTAR*, Alexander et al. (2013) found an abundance of mildly obscured quasars selected at $\gtrsim 10$ keV ($L_{10-40\,keV} > 10^{44}$ erg s^{-1}, $N_H \gtrsim 10^{22}$ cm^{-2}), but none with $N_H > 10^{24}$ cm^{-2}, thus limiting the fraction of CT quasars (CT QSOs) above 10 keV to $\lesssim 33$% over $z = 0.5$–1.1. In parallel, a pilot *NuSTAR* study of three $z \approx 0.5$ SDSS-QSO2 selected as being CT candidates could not confirm the presence of CT obscuration in any, despite the significantly improved hard-band sensitivity with respect to prior *Chandra* and *XMM-Newton* constraints (Lansbury et al. 2014), emphasizing the difficulty of studying distant obscured AGNs.

Here, we present *NuSTAR* observations of the first target in an extended SDSS-QSO2 sample, for which the selection is designed to provide the best *direct* constraints possible on the most obscured SDSS-QSO2s. The source, Mrk 34, is a known Type 2 AGN with narrow permitted and forbidden emission lines (Heckman et al. 1981; Dahari & De Robertis 1988). A recent, detailed multi-component fit to the SDSS nuclear spectrum finds a maximal velocity component with FWHM of ≈ 616 km s^{-1} to the Hα and Hβ permitted lines and the forbidden [O III] and [N II] doublets (Mullaney et al. 2013).[27] The observed line power $L_{[O\,III]} = 10^{8.8} L_\odot$ is comparable to the mean luminosity of radio-quiet Palomar-Green quasars at $z \lesssim 0.5$ (Boroson & Green 1992). The source is radio-quiet with a small-scale jet of extent 3.7 kpc, bipolar radio morphology ending in two hot spots, and evidence of interaction between the jet and the narrow-line region clouds (Ulvestad & Wilson 1984; Falcke et al. 1998; Fischer et al. 2013). In the infrared, the source has a total power of $L_{8-1000\,\mu m} \approx 2 \times 10^{11} L_\odot$ (González Delgado et al. 2001) and lies in the luminosity regime associated with luminous infrared galaxies (LIRGs). It is also a known luminous H$_2$O megamaser source, which is usually associated with the presence of significant circumnuclear absorption (Henkel et al. 2005; Kondratko et al. 2006; Greenhill et al. 2008).

X-ray spectroscopy of Mrk 34 with *XMM-Newton* found a strong Fe Kα fluorescence emission line (Greenhill et al. 2008; Jia et al. 2013). The megamaser and the strong Fe line suggest the presence of CT material in the source, but this has not been possible to prove with data below 10 keV alone. The *XMM-Newton*-detected continuum is that of a Compton-thin ($N_H < 10^{24}$ cm^{-2}) AGN when fitted with an absorbed power law (PL). In the *NuSTAR* data presented herein, we detect the source to $\sim$40 keV. The high-quality spectra unambiguously show, for the first time in an SDSS-selected QSO2, evidence for a reflection-dominated continuum requiring CT absorption along the line of sight. This demonstrates the gain that *NuSTAR* is providing for obscured AGN studies.

The source redshift is $z = 0.051$, giving a luminosity distance of 236 Mpc for a flat cosmology with $H_0 = 67.3$ km s^{-1} Mpc^{-1} and $\Omega_\Lambda = 0.685$ (Planck Collaboration et al. 2013). All fit uncertainties are quoted at 90% confidence, unless stated

---

[27] An extra highly broadened component is reported in their fit with FWHM = 11989.1 km s^{-1}, but is not significant.

otherwise. An outline of this paper is as follows. Section 2 describes our target selection strategy and Section 3 contains details of our X-ray observations and reduction. The spectral fitting procedures and results from the *NuSTAR* data, both alone and when combined with *XMM-Newton*, are described in Sections 4 and 5, respectively. In Section 6, we discuss the intrinsic source properties and how Mrk 34 fits in the context of bona fide CT AGNs and the QSO2s population in general. The paper concludes with a summary in Section 7.

2. TARGET SELECTION

Mrk 34 was chosen as a promising target for *NuSTAR* from the samples of SDSS-QSO2s that have prior X-ray follow-up observations (Vignali et al. 2006, 2010; Jia et al. 2013). By fitting *XMM-Newton* data of the source, Jia et al. (2013) found an observed (absorbed) $L_{2-10} = 9 \times 10^{41}$ erg s^{-1} and $N_{\rm H} = 2.63^{+4.21}_{-2.63} \times 10^{23}$ cm^{-2} (consistent with an upper limit of $N_{\rm H} < 6.84 \times 10^{23}$ cm^{-2}). In addition, Mrk 34 showed the following characteristics associated with heavy or CT X-ray obscuration.

1. As compared to the observed power in the [O III] emission line ($L_{\rm [O\,III]} = 10^{8.8} L_\odot$; Reyes et al. 2008), the observed 2–10 keV power is low: $L_{2-10}/L_{\rm [O\,III]} = 0.4.$[28] This ratio places Mrk 34 at about 200 times lower in L_{2-10} than the local Type 1 AGN correlation between L_{2-10} and $L_{\rm [O\,III]}$ (Mulchaey et al. 1994; Netzer et al. 2006; Panessa et al. 2006).

2. The source also shows a low observed $L_{2-10}/L_{12\,\mu m}$ ratio that places it $\approx 100\times$ below the correlation (in terms of L_{2-10}) presented in Gandhi et al. (2009). The infrared luminosity is $L_{12\,\mu m} = 2(\pm 0.04) \times 10^{44}$ erg s^{-1}, measured as λL_λ, from linear interpolation of multi-band all-sky catalog data produced by the *WISE* mission to a rest-frame wavelength of 12 μm (Wright et al. 2010);

3. Finally, the *XMM-Newton* data show a strong Fe Kα equivalent width (EW$_{\rm K\alpha}$) = $1.6^{+0.9}_{-0.8}$ keV (Jia et al. 2013; Greenhill et al. 2008).

Jia et al. (2013) determined an intrinsic X-ray luminosity $L_{2-10,\rm in} = 2 \times 10^{42}$ erg s^{-1} after correcting for the obscuring column of $N_{\rm H} \approx 3 \times 10^{23}$ cm^{-2} measured in the *XMM-Newton* data below $\sim$10 keV. Using physical reflection model fits to the same data, LaMassa et al. (2014) constrained $N_{\rm H} > 4 \times 10^{23}$ cm^{-2}, implying a factor of a few larger luminosity, $L_{2-10,\rm in} = 9^{+6}_{-4} \times 10^{42}$ erg s^{-1}. By contrast, using either $L_{\rm [O\,III]}$ or $L_{12\,\mu m}$ (points 1 and 2 above) as an indirect proxy of the intrinsic power would imply $L_{2-10,\rm in} \sim 10^{44}$ erg s^{-1}, about 10 times higher still. In addition, the value of EW$_{\rm K\alpha} \gtrsim 1$ keV above classifies Mrk 34 as a CT candidate, which would also imply the need for strong corrections to the observed luminosity. This can be tested using higher energy X-ray data.

The source is not detected by the *Swift*/BAT all-sky survey at the nominal 70 month survey 4.8σ sensitivity flux limit of $F_{14-195} = 1.3 \times 10^{-11}$ erg s^{-1} cm^{-2} (Baumgartner et al. 2013). However, direct examination of the BAT maps reveals a 3.7σ excess at the position of Mrk 34 (for details on the maps and the procedure, see Koss et al. 2013). Extrapolation of the observed *XMM-Newton* continuum to hard X-rays using typical reflection models (described below) also implied a

good detection probability with *NuSTAR* in modest exposure times. Therefore, the object was chosen as a promising *NuSTAR* target.

3. OBSERVATIONS

3.1. NuSTAR

Mrk 34 was observed on UT2013-09-19 (ObsID 60001134002) for an on-source time of 25.7 ks. The data were processed with the *NuSTAR* Data Analysis Software (NUSTARDAS) v.1.3.0 within HEASOFT v.6.15.1. With the *NuSTAR* UT2013-05-09 CALDB release, calibrated and cleaned event files were produced using the NUSTARDAS task nupipeline with standard filter flags. Passages of the satellite through the South Atlantic Anomaly were filtered out and the standard depth cut used to help reduce instrumental background. Spectra and response files were extracted using the nuproducts task. The net exposure time was approximately 23.9 ks.

A 45″ radius aperture was used for extracting source counts. Background counts were extracted from a neighboring, off-target circular aperture 100″ in radius, free of any other sources. Using a source-centered annular region to define the background gave consistent results.

3.2. XMM-Newton

Archival *XMM-Newton* observations (ObsID 0306050701) obtained through a medium filter in full-window mode from UT2005-04-04 were reduced and analyzed using standard procedures within SAS v13.0.0.[29] Spectra were extracted within a 15″–radius aperture. The spectra and responses from the two EPIC MOS detectors were combined using the addascaspec script as they were very similar. The net good exposure time is 8.8 ks (PN) and 22.9 ks (combined MOS). We note that there are no other bright sources within $\sim$1.′5 of the target position in the *XMM-Newton* (and *NuSTAR*) images. More details on these *XMM-Newton* data can be found in Jia et al. (2013) and LaMassa et al. (2014).

4. X-RAY SPECTRAL FITTING

We began with an examination of the *NuSTAR* data alone. Mrk 34 is well-detected in both focal plane modules (FPMs), with net count rates of 7.5($\pm$0.7) $\times 10^{-3}$ counts s^{-1} in FPMA and 7.9($\pm$0.8) $\times 10^{-3}$ counts s^{-1} in FPMB, respectively, over the energy range $\approx$3–40 keV. The extracted spectra are shown in Figure 1. Spectral analysis was carried out over this energy range using XSPEC v.12.8.1 (Arnaud 1996). All spectra have been grouped to a minimum of 20 counts per bin.

A prominent excess of counts just above 6 keV suggests the presence of Fe Kα emission. Parameterizing the data with a PL continuum and a Gaussian line with fixed rest-frame line centroid energy $E = 6.40$ keV and redshift $z = 0.051$ returns a photon index $\Gamma = 0.15^{+0.45}_{-0.16}$ (where photon flux density $N_E \propto E^{-\Gamma}$), and EW$_{\rm K\alpha} = 1.9^{+2.3}_{-0.8}$ keV with a fit statistic of $\chi^2 = 29.9$ for 23 degrees of freedom (dof). The confidence ranges on EW$_{\rm K\alpha}$ are determined by drawing an ensemble of 10,000 parameter values from the fit. Letting the line centroid float freely returns a rest-frame energy of $E = 6.6^{+0.1}_{-0.3}$ keV, which shows that this is consistent with neutral Fe Kα (although weaker Fe Kβ or higher ionization lines are likely to be contributing). The observed fluxes are $F_{2-10} = 1.9^{+0.1}_{-1.0} \times 10^{-13}$ erg s^{-1} cm^{-2}

---

[28] No luminosity uncertainties are stated by Jia et al. (2013). From our spectral fit, we estimate a 25% uncertainty on L_{2-10}, which will dominate the error in the $L_{2-10}/L_{\rm [O\,III]}$ ratio.

[29] http://xmm.esa.int/sas
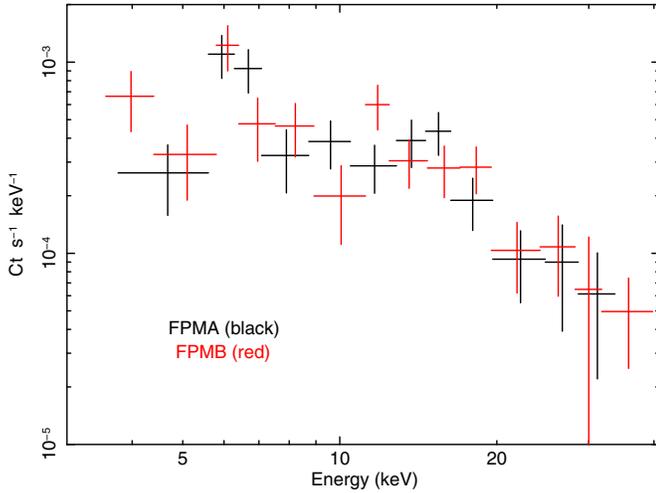
Figure 1. Background-subtracted *NuSTAR* spectra of Mrk 34 for the two FPMs. (A color version of this figure is available in the online journal.)

and $F_{10-30} = 1.1^{+0.1}_{-0.5} \times 10^{-12}$ erg s^{-1} cm^{-2}, respectively. The very flat Γ and large EW$_{K\alpha}$ are characteristic signatures of reflection from optically thick cold gas.

Over the common energy range of $\sim$3–10 keV, *XMM-Newton* gives consistent results with *NuSTAR* on spectral shape, fluorescence strength, and continuum normalization: $\Gamma = 0.17 \pm 0.51$, EW$_{K\alpha} = 2.1^{+3.2}_{-1.0}$ keV, $F_{2-10} = 1.7^{+0.2}_{-1.0} \times 10^{-13}$ erg s^{-1} cm^{-2}. This consistency implies that there has been no significant variability between the two observations. We therefore proceeded to fit more physical reflection models to the combined *NuSTAR* and *XMM-Newton* data. We used two physically motivated and self-consistent reflection models for the hard X-ray regime, in addition to including other common spectral components at soft energies. These are described below.

4.1. MYTORUS: Model M

The MYTORUS model simulates a toroidal absorber geometry with a covering factor of 0.5 (a fixed half-opening angle $\theta_{tor} = 60°$) centered on a continuum source (Murphy & Yaqoob 2009). It self-consistently includes (1) distortion of the zeroth-order transmitted component (which is a PL in our case) due to photoelectric absorption and Compton scattering, (2) Compton-scattering off the torus, and (3) associated fluorescence line emission (neutral Fe Kα at 6.4 keV and Kβ at 7.06 keV) and the Compton shoulder to the fluorescence lines. We used MYTORUS mainly in the standard ("coupled") mode where the normalizations of these three components are tied to the intrinsic continuum, effectively coupling N_H(los) to the torus inclination angle. Table grids with an equatorial column density (N_H(eq)) of up to 10^{25} cm^{-2} are available and defined between 0.5–500 keV. This model is referred to as "model M."

MYTORUS also allows for the decoupling of the column density from geometry, and N_H(los) from that responsible for the scattered continuum (N_H(scatt)). Such a "decoupled" mode fit is briefly described in Section 6.1.

4.2. TORUS: Model T

The TORUS model of Brightman & Nandra (2011) allows changing geometries through variable θ_{tor}, but, through the torus, N_H(los) is defined such that it is independent of inclination (θ_{inc}). Table models with N_H up to 10^{26} cm^{-2}, or about 10 times more than allowed in MYTORUS, are publicly available. TORUS

also includes Compton scattering and Fe Kα fluorescence. It is defined between 0.1–320 keV, which enables us to extend the fit to lower energies as compared to MYTORUS. This model is referred to as "model T."

4.3. Other Spectral Components

The low-energy ($\lesssim$2 keV) spectral shape as seen with *XMM-Newton* is much softer than the continuum shape at higher energies (Jia et al. 2013; LaMassa et al. 2014). This was parameterized as hot gas plasma emission in the host galaxy with APEC (Smith et al. 2001) and included in both models M and T. Two such APEC components were found to be necessary for both models. Additional emission from an optically thin medium on larger scales in the host galaxy, which scatters AGN emission into the line of sight, may be present as could emission from X-ray binaries. Such emission was simulated using a single PL (of photon-index Γ tied to that of the AGN) with a scattering fraction, f_{scatt}, relative to the intrinsic PL and obscured by an additional gas column (N_H(host)), which is independent of the column associated with the torus. Such components are often used to describe the soft emission observed in obscured AGNs (e.g., Done et al. 2003), but in the absence of high spectral resolution soft X-ray data, these are only meant as a simple prescription to describe the spectral shape in this regime. We will discuss whether such components are viable in Section 6.3, together with other physical models of the soft emission.

All abundances for the torus models and the thermal components are fixed at solar.

PHABS absorption through a fixed low Galactic column, N_H(Gal) = 6.8×10^{19} cm^{-2}, of cold gas, based upon H I measurements along the line of sight (Dickey & Lockman 1990), was also included in all spectral fits. Finally, a cross-calibration constant between the two missions was included as a free parameter. Cross-calibration of the *XMM-Newton* EPIC MOS and pn cameras has shown that these instruments are in very good agreement with each other when fitting over their full energy range (Kirsch et al. 2004), so we fixed their relative cross-normalization to one.

The final models have the following notations in XSPEC, with explanatory mappings in square brackets:

MODEL M = CONST × PHABS$[\mapsto N_H^{Gal}]$
$\quad$ × ZPHABS$[\mapsto N_H^{host}]$ × (APEC(×2)
$\quad$ + POW ∗ ETABLE{mytorus_Ezero_v00.fits}
$\quad$ + ATABLE{mytorus_scatteredH500_v00.fits}
$\quad$ + ATABLE{mytl_V000010nEp000H500_v00.fits}
$\quad$ + CONST$[\mapsto f_{scatt}]$ × POW),

and

MODEL T = CONST × PHABS$[\mapsto N_H^{Gal}]$
$\quad$ × ZPHABS$[\mapsto N_H^{host}]$ × (APEC(×2)
$\quad$ + POW ∗ ATABLE{torus1006.fits}
$\quad$ + CONST$[\mapsto f_{scatt}]$ × POW).

5. RESULTS FROM COMBINED *NuSTAR* AND *XMM-NEWTON* FITS

We first fitted the broadband *NuSTAR* and *XMM-Newton* data using the coupled MYTORUS model M. A fit was found with reflection *dominating* at all energies above $\sim$3 keV. This
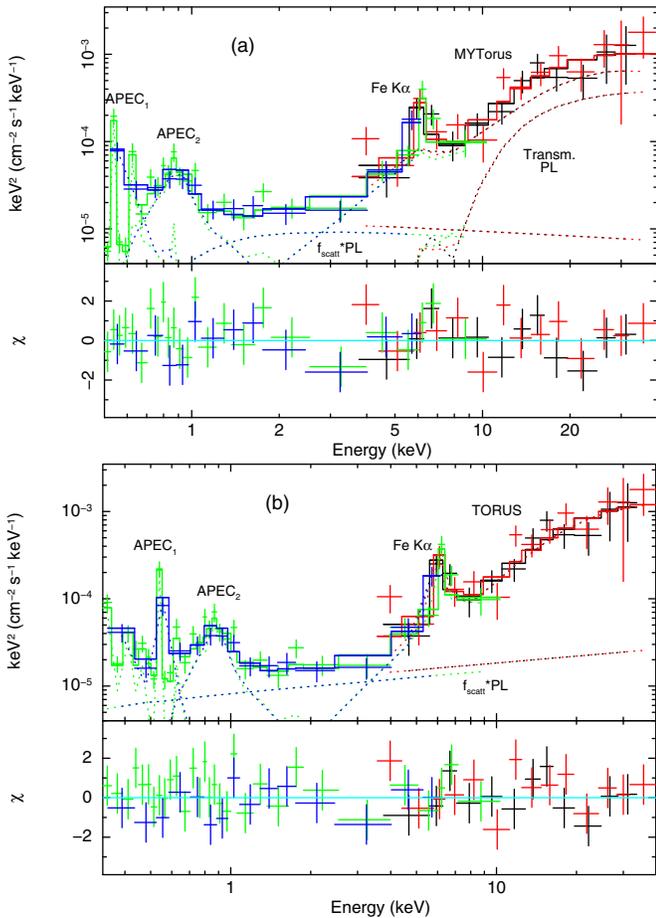
Figure 2. X-ray fits to the combined *NuSTAR* and *XMM-Newton* data. Shown in EF_E units are (a) the unfolded model M and (b) model T fits, respectively. The bottom panels show the residuals in terms of sigmas with error bars of size one. The transmitted PL is not treated separately in the TORUS model T. Color scheme: black (FPMA), red (FPMB), green (pn), blue (MOS1+2). The MYTORUS fit was restricted to energies above 0.5 keV, which is the lower end of the range over which it is defined.

(A color version of this figure is available in the online journal.)

is shown in Figure 2 and the best-fit parameters are listed in Table 2. The fit returned an equatorial column, $N_H(eq) \approx 10^{25}$ cm^{-2}. The inclination angle lies between $\approx 60°$ and $75°$, constrained at the lower end by the opening angle of the torus. $N_H(eq)$ lies well within the CT regime. In the coupled MYTORUS model, the line-of-sight column is tied to $N_H(eq)$ and θ_{inc} from the model geometry and $N_H(los) \approx 2.5 \times 10^{24}$ cm^{-2} for the best-fit value of $\theta_{inc} \approx 61°$. The upper model threshold of 10^{25} cm^{-2} is permitted by the fit, i.e., N_H is unconstrained at the upper end.

The absorbed luminosity over 2–10 keV is $L_{2-10} = 1.2 \times 10^{42}$ erg s^{-1}, and over a broader energy range of 0.5–30 keV covering both *NuSTAR* and *XMM-Newton* is $L_{0.5-30} = 8.8 \times 10^{42}$ erg s^{-1}. Correcting for absorption implies $L_{2-10, in} \approx 6 \times 10^{43}$ erg s^{-1} and $L_{0.5-30,in} \approx 1.5 \times 10^{44}$ erg s^{-1}, respectively. The observed EW$_{K\alpha} \approx 1.2$ keV, as expected for a reflection-dominated spectrum.[30] The fitted $\Gamma \approx 2.2$ is somewhat steep compared to the mean $\langle\Gamma\rangle \sim 1.9$ measured in high-quality AGN data (e.g., Nandra et al. 1997; Mateos et al. 2005; Piconcelli et al.

---

[30] Measured by numerical integration of the best-fit Fe Kα line plus Compton shoulder model flux and divided by the total fitted MYTORUS continuum interpolated to 6.4 keV rest-frame.

2005), but not extraordinarily so within the allowed confidence range.

The softest energies can be parameterized using two APEC components and optically thin scattering. The temperatures (kT) of the APEC components are ≈ 0.1 and 1 keV, respectively. Removing either APEC component results in a $\Delta\chi^2$ of at least +50 for two additional dof, implying that both are required. The luminosity associated with the two APEC components is $L_{0.5-2}^{APEC} \approx 4 \times 10^{41}$ erg s^{-1}. The scattering normalization $f_{scatt} \sim 0.3\%$, which gives a luminosity of $L_{2-10}^{scatt} \sim 10^{41}$ erg s^{-1}. The *XMM-Newton*-to-*NuSTAR* cross-calibration constant is lower than (but consistent with) approximately one.

Notice that the best-fit $N_H(eq)$ and θ_{inc} values are at the upper and lower extremes, respectively, allowed in MYTORUS for an obscured line of sight intersecting the torus. This suggests that there is some tension in the fit between the conflicting need to strongly suppress the intrinsic continuum at all energies (i.e., a large N_H) and the need for an unabsorbed reflection-dominated continuum and strong Fe Kα line below 10 keV (which pushes θ_{inc} down). This is not easy to simulate within MYTORUS, because of its geometrically constrained configuration. Removing one dof by fixing θ_{inc} to $75°$ (at the high end of the allowed confidence range in the above fit) also yields an acceptable solution with $N_H(los) = 3 \times 10^{24}$ cm^{-2} and $L_{2-10, in} = 1.7 \times 10^{44}$ erg s^{-1}.

Model T gives us the opportunity to examine systematically different torus model assumptions and geometries, particularly through its allowance of varying opening torus angles. We found that it was not possible to simultaneously constrain both θ_{inc} and θ_{tor}. We thus decided to fix $\theta_{inc} = 87°$, corresponding to an edge-on inclination. The strong megamaser in Mrk 34 provides some justification for this choice, as most megamasers are associated with edge-on inclinations (Kuo et al. 2011). This choice also allows for an examination of the effect of a larger θ_{inc} than that preferred by MYTORUS. In addition, the fit for θ_{tor} is then no longer restricted by θ_{inc}, because the model allows for θ_{tor} values up to $84°$ (Brightman & Nandra 2011).

Model T yields an excellent fit, with a flatter $\Gamma \approx 1.7$ (Table 2 and Figure 2). The best-fit $N_H(los)$ lies above 10^{25} cm^{-2} with a lower 90% confidence interval allowing $N_H(los) > 3.5 \times 10^{24}$ cm^{-2}. This is again within the CT regime and unconstrained at the high end, this time up to 10^{26} cm^{-2}. In this case, EW$_{K\alpha} \approx 1.4$ keV. A broad range of torus opening angles is allowed, $27 \lesssim \theta_{tor} \lesssim 78°$. Small θ_{tor} values are equivalent to large torus solid angles, which can produce stronger reflection and fluorescence components. On the other hand, very thin tori ($\theta_{tor} > 78°$ in our fits) do not produce enough reflection. Whereas model M requires some host absorption ($N_H(host) \approx 6 \times 10^{21}$ cm^{-2}), this is partly driven by the fitted steep Γ value and is not needed for model T.

Finally, we note that using the PEXRAV (Magdziarz & Zdziarski 1995) or PEXMON (Nandra et al. 2007) reflection models as alternatives to the torus models above give broadly similar results in terms of the requirement of a reflection-dominated continuum. In fact, reflection-only models (R value of less than 0) yield fully acceptable fits (with reduced $\chi^2 \approx 1$) without the need for a direct component. These models are not described in detail here because they simulate reflection off a slab geometry and assume an infinite optical depth, neither of which are likely to represent the torus. There is also no strong constraint on the intrinsic luminosity in such a scenario because the reflector and obscurer are disjoint and the solid angle of the reflecting surface visible to us is unknown.

6. DISCUSSION

Mrk 34 was selected for *NuSTAR* observation because previous low-energy X-ray follow-up provided indirect evidence of high or CT obscuration, including low $L_{2-10}/L_{[\text{O\,III}]}$ and low $L_{2-10}/L_{12\,\mu\text{m}}$ ratios relative to Type 1 AGNs, as well as an $\text{EW}_{K\alpha} > 1$ keV. In terms of its optical spectral properties, in particular its narrow-line luminosity ($L_{[\text{O\,III}]} = 10^{8.8}\,L_\odot$), Mrk 34 is quite representative of the large sample of 887 SDSS-QSO2s compiled by Reyes et al. (2008) whose distribution has an average $\langle L_{[\text{O\,III}]} \rangle = 10^{8.7}\,L_\odot$ (with a 1σ scatter of 0.4 dex). With *NuSTAR*, we find *direct* evidence of CT obscuration in the form of a flat hard X-ray (3–40 keV) continuum, which can be modeled as arising from reflection off optically thick circumnuclear gas self-consistently with the strong neutral Fe line.

Although the source was selected from optical spectroscopy, the derived intrinsic X-ray power also places Mrk 34 in (or very near) the regime associated with obscured X-ray quasars ($L_{2-10,\,\text{in}} \gtrsim 10^{44}$ erg s^{-1}). Whereas local CT Seyfert 2s have been studied at lower X-ray luminosities for many years, this is the first time that such a robust measurement of the intrinsic X-ray power is possible for a powerful SDSS-selected QSO2. Mrk 34 is thus a "gold standard" CT QSO2, satisfying all the above characteristics typically associated with this class.

6.1. On the Intrinsic Power and Obscuring Column Density

The two broadband *NuSTAR+XMM-Newton* model fits in Table 2 require $N_{\text{H}}(\text{los}) \gtrsim 2 \times 10^{24}$ cm^{-2} although much higher values of N_{H} are allowed. The photon indices of the two fits also allow for some variation in the intrinsic PL slope. Despite these uncertainties, it is noteworthy that the corresponding absorption-corrected X-ray luminosities of the two model fits differ only by a factor of two, at $L_{2-10,\,\text{in}} \sim (0.6\text{--}1.2) \times 10^{44}$ erg s^{-1}. This is a consequence of the fact that the observed hard X-ray spectrum is dominated by the reflection component at all energies, so the modeled intrinsic luminosity is mainly dependent upon the observed flux and the covering factor of the reflector and is less sensitive to the reflecting gas column or the intrinsic PL shape that produces the reflection spectrum. In other words, the model fits likely provide a good estimate of the intrinsic power of the AGN, but only a lower limit on the torus column density.

A systematically different obscuring geometry could yield a different result, of course, and this may be investigated using the "decoupled" mode of MYTORUS (Murphy & Yaqoob 2009). With differing normalizations and/or column densities for the transmitted and scattered components, this mode can be interpreted as an approximate parameterization of alternate geometries such as a patchy torus or of differing elemental abundances. However, it is difficult to constrain such decoupled models for Mrk 34 because the intrinsic continuum is not obviously visible at any energy, leading to a large degeneracy on the reflection fraction. In fact, including separate edge-on and face-on scattering/fluorescence components with a free multiplicative scaling between them in the MYTORUS fit (as recommended by Yaqoob 2012) leads to the scattering component completely dominating over the intrinsic PL by large factors ($\sim$100) suggesting much higher values of $N_{\text{H}}(\text{los})$ than the lower confidence ranges that we presently constrain.

Additional checks on the intrinsic power can be provided by indirect multiwavelength relations. These are shown in
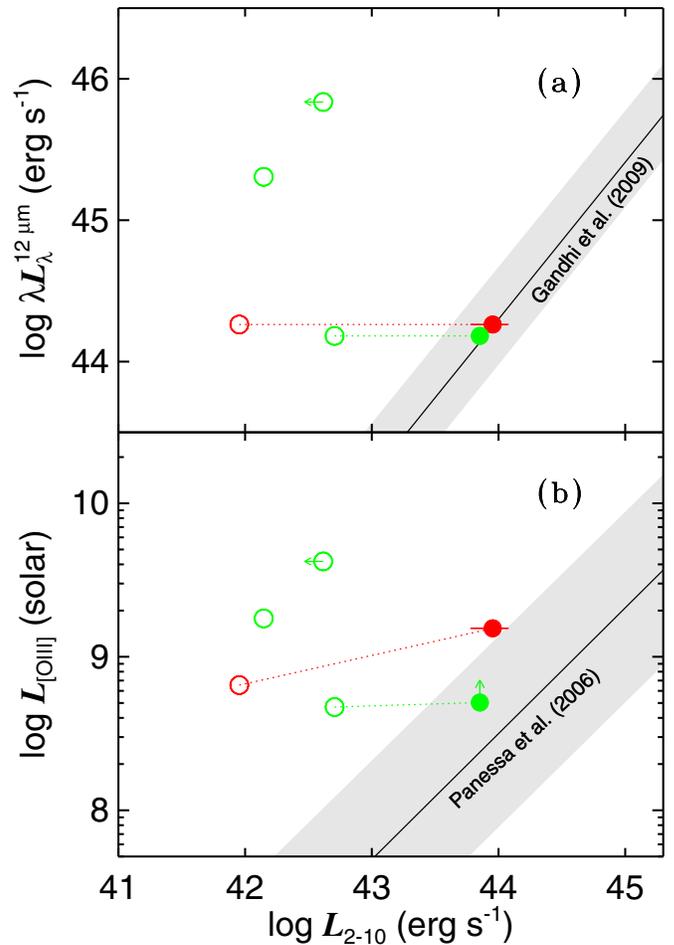
Figure 3. Multiwavelength correlations: (a) $L_{12\,\mu\text{m}}$ vs. L_{2-10} and (b) $L_{[\text{O\,III}]}$ vs. L_{2-10}, for Mrk 34 (red) and the three other *NuSTAR*-observed QSO2s from Lansbury et al. (2014, green). Open symbols denote observed luminosities. Filled symbols denote intrinsic values for the two *NuSTAR*-detected sources (Mrk 34 in red and SDSS J0011+0056 in green). These are corrected for obscuration and reddening as described in the text. For Mrk 34, the plotted X-ray luminosity is the mean of the two model best-fit values of $L_{2-10,\,\text{in}}$ in Table 2, with the uncertainty denoting the range between them. The upward-pointing arrow for SDSS J0011+0056 denotes the fact that the Balmer decrement and narrow-line-region reddening correction estimate are not available in this case. The shaded zones denote the 1σ relation scatters of ≈ 0.3 and 0.6 dex, respectively.

(A color version of this figure is available in the online journal.)

Figure 3, the top panel of which plots the $L_{12\,\mu\text{m}}$ versus L_{2-10} relation for Mrk 34 along with the three other SDSS-QSO2s observed by *NuSTAR* thus far (Lansbury et al. 2014). The latter objects were selected from sources at $z \sim 0.4$–0.5 with $L_{2-10}/L_{[\text{O\,III}]} < 2.5$ and sample a range of about one dex in $L_{[\text{O\,III}]}$. The intrinsic L_{2-10} for Mrk 34 matches well with the infrared–X-ray luminosity relation by Gandhi et al. (2009), lying within the 1σ relation scatter. The same holds true when using other relations published in Gandhi et al. (2009) and Asmus et al. (2011), which effectively include varying levels of host galaxy contamination to the mid-infrared. Although high angular resolution infrared imaging (e.g., Asmus et al. 2014) is not available for Mrk 34, we note that the *WISE* mid-infrared color of the source from the all-sky catalog is $W1 - W2 = 1.18 \pm 0.03$, placing the source comfortably inside the color zone identified by Stern et al. (2012), where the mid-infrared flux is likely to be AGN-dominated. In other words, the close match to the correlation

Table 1
Mrk 34 Luminosities

Band and Quantity	10^{43} erg s^{-1}
$L_{0.5-2,\text{in}}$	0.02
L_{2-10} (absorbed)	0.12
$L_{0.5-30}$ (absorbed)	0.88
L_{10-40} (absorbed)	1.02
$L_{2-10,\text{in}}$[a]	6–12
$L_{0.5-30,\text{in}}$[a]	15–31
$L_{10-40,\text{in}}$[a]	4–15
$L_{[\text{O III}]}$ (reddened)	0.24
$L_{[\text{O III}]}$ (dereddened)	0.56
$\lambda L_{\lambda}(12\,\mu\text{m})$	20
$L_{8-1000\,\mu\text{m}}$	80
$L_{\text{H}_2\text{O}}$	0.5×10^{-7}

Note. [a] Ranges refer to the absorption-corrected values for the AGN continuum between models M and T.

in the top panel of Figure 3 is entirely attributable to the AGN power alone.

The same figure also shows the $L_{[\text{O III}]}$ versus L_{2-10} plane. Mrk 34 lies at the threshold of the 1σ scatter of the relation defined by Panessa et al. (2006), and the source position is approximately similar with respect to the mean and scatter defined by other relations (e.g., Netzer et al. 2006). *Intrinsic* [O III] luminosities are also shown for the two *NuSTAR*-detected sources and are corrected for Galactic reddening (Schlafly & Finkbeiner 2011). For Mrk 34, we were able to additionally correct for reddening in the narrow-line region of the host galaxy, following the procedure of Bassani et al. (1999). For this, we measured the Balmer decrement from the Hα and Hβ narrow line fluxes provided by the SDSS spZline pipeline output (Bolton et al. 2012). A ratio of $F_{\text{H}\alpha}/F_{\text{H}\beta} = 3.98 \pm 0.03$ is measured,[31] which translates into an [O III] dereddening factor of 2.3. This correction is not possible for the sources from Lansbury et al. (2014) because their higher redshift means that Hα lies beyond the SDSS wavelength range. According to the bottom panel of Figure 3, there is a mild suggestion that Mrk 34 may have a higher L_{2-10} still, but it is difficult to provide a precise cross-check given the large scatter associated with most $L_{[\text{O III}]}$:L_{2-10} correlations.

Finally, with an isotropic megamaser power, $L_{\text{H}_2\text{O}} \sim 10^3\,L_{\odot}$ (Henkel et al. 2005), Mrk 34 now also lies within the scatter of the possible relationship between $L_{\text{H}_2\text{O}}$ and L_{2-10} proposed by Kondratko et al. (2006). These authors identified two maser complexes in Mrk 34 that are consistent with symmetric blue- and redshifted high-velocity ($\sim$500 km s^{-1}) emission. This is consistent with maser excitation resulting from X-ray irradiation of accretion disk gas. Higher intrinsic X-ray luminosities would push the source beyond the scatter of the proposed $L_{\text{H}_2\text{O}}$:L_{2-10} relation.

In short, these multiwavelength comparisons suggest that our X-ray spectral analysis reliably captures the intrinsic X-ray power of Mrk 34. A compilation of luminosities from our *NuSTAR* modeling and over the various wavelength bands discussed above is presented in Table 1.

6.2. On the Bolometric Luminosity and Eddington Ratio

When compared to the total infrared power of $L_{8-1000} \approx 2 \times 10^{11}\,L_{\odot} = 8 \times 10^{44}$ erg s^{-1} as probed by *IRAS*, $L_{2-10,}/L_{8-1000} = 0.08$–0.15. For any typical AGN bolometric correction factor, $L_{\text{Bol}}/L_{2-10} \approx 10$–30 (e.g., Elvis et al. 1994; Vasudevan et al. 2010), the AGN easily has enough power to drive the bulk of the infrared emission. LIRGs (with $10^{11}\,L_{\odot} < L_{8-1000} < 10^{12}\,L_{\odot}$) generally show a much lower fractional AGN contribution to the infrared (e.g., Alonso-Herrero et al. 2012), and Mrk 34 appears to be more similar to Palomar-Green QSOs in this respect (Veilleux et al. 2009). The high current luminosity of Mrk 34 may simply represent an upward fluctuation in an otherwise more modest accretion history (e.g., Hickox et al. 2014), although a significant ongoing gas accretion rate is required in order to drive the observed power: $\dot{M} = L_{\text{Bol}}/\eta c^2 \approx 0.2$–0.3 $M_{\odot}$ yr^{-1} (assuming an X-ray bolometric correction of 15 and accretion efficiency $\eta = 0.1$).

There is no secure measurement of the supermassive black hole mass (M_{BH}) for Mrk 34 as yet. Although a megamaser has been detected, there is no corresponding spatially resolved map; therefore, its inner radius is unknown. However, if we assume that the megamaser disk in Mrk 34 has an inner radius of $\sim$0.1–0.5 pc as seen in other nearby sources (e.g., Kuo et al. 2011), the observed 500 km s^{-1} maser velocity (Kondratko et al. 2006) would imply $M_{\text{BH}} \sim (0.6$–3$) \times 10^7\,M_{\odot}$. Extrapolating the galaxy stellar velocity dispersion (σ) from the [O III] emission line width and using the M_{BH}–σ relation from Tremaine et al. (2002), Wang et al. (2007) instead estimate $M_{\text{BH}} = 10^{7.96}\,M_{\odot}$. On the other hand, Oh et al. (2011) measure $\sigma = 123 \pm 5$ km s^{-1} from their analysis of the SDSS spectra, and using this velocity dispersion together with the updated M_{BH}–σ relation from McConnell & Ma (2013) would imply that $M_{\text{BH}} = 10^{7.12 \pm 0.38}\,M_{\odot}$.

If we assume that a range of $M_{\text{BH}} = 10^{7-8}\,M_{\odot}$ reasonably encompasses the current uncertainty on M_{BH}, and combine the intrinsic X-ray power that we measure with the typical AGN bolometric correction factors quoted above, we find that the AGN is radiating at an Eddington fraction of $\approx$0.05–2.5.

Better data are clearly needed for more precise measurements of M_{BH}. A very long baseline interferometry map of the megamaser would resolve the inner disk radius, and hence provide a measure of M_{BH}. At the distance of Mrk 34, a physical scale of 0.5 pc corresponds to an angular size of $\approx$0.48 mas, which is within range of the synthesized beam sizes currently available (Kuo et al. 2011). Alternatively, high-quality near-infrared imaging with the *Hubble Space Telescope* (*HST*) or the future *James Webb Space Telescope* could provide a complementary measurement of M_{BH} through accurate measurement of the bulge mass and the known correlation between the two quantities (e.g., Marconi & Hunt 2003).

6.3. On the Origin of the Soft X-Ray Emission

The soft X-ray emission of Mrk 34 is interesting because of the presence of high-luminosity components, which steepen the overall source spectrum significantly below $\sim$3 keV (Figure 2). In fact, the first published X-ray detection of Mrk 34 appears to have been from the *ROSAT* High Resolution Imager sensitive over the range of 0.1–2.4 keV, rather than at harder X-rays (Pfefferkorn et al. 2001).

Two APEC components are used to parameterize the soft X-rays below 1 keV and a PL simulating scattering by diffuse plasma dominates around 2 keV (Figure 2 and Table 2).

---

[31] It is worth noting that this Balmer decrement is much milder than the value of $F_{\text{H}\alpha}/F_{\text{H}\beta} = 10.47$ according to Dahari & De Robertis (1988), which may be a result of differing slit positioning and setup. We use the more recent SDSS measurements here.

Table 2
X-Ray Spectral Fits

Component	Parameter	Model M	Model T	Units
APEC$_1$	kT_1	0.18 ± 0.03	$0.11^{+0.03}_{-0.02}$	keV
	$L_{0.5-2}$	2.0	1.6	$\times 10^{41}$ erg s^{-1}
APEC$_2$	kT_2	0.96 ± 0.10	$0.93^{+0.07}_{-0.13}$	keV
	$L_{0.5-2}$	2.4	2.2	$\times 10^{41}$ erg s^{-1}
MYTORUS/TORUS	$N_H(\mathrm{eq})$	$9.51^{+u}_{-4.17}$	$\cdots$	$\times 10^{24}$ cm^{-2}
	$N_H(\mathrm{los})$	$2.45^{+u}_{-1.08}$	$35.5^{+u}_{-31.9}$	$\times 10^{24}$ cm^{-2}
	θ_{inc}	$61^{+14}_{-0.5}$	87^f	deg
	θ_{tor}	$\cdots$	67^{+11}_{-40}	deg
	EW(Fe Kα)	1.2	1.4	keV
AGN continuum	Γ	$2.2^{+0.2}_{-0.3}$	$1.7^{+0.4}_{-0.5}$	
	L_{2-10}	0.6	1.2	$\times 10^{44}$ erg s^{-1}
	$L_{0.5-30}$	1.5	3.1	$\times 10^{44}$ erg s^{-1}
Diffuse scattering	f_{scatt}	$3.5^{+2.2}_{-1.4}$	$2.2^{+2.1}_{-1.8}$	$\times 10^{-3}$
Large-scale absorption	$N_H(\mathrm{host})$	$4.4^{+0.4}_{-0.1}$	$\cdots$	$\times 10^{21}$ cm^{-2}
XMM:NuSTAR cross-calib	CONST	$0.84^{+0.32}_{-0.20}$	$0.83^{+0.21}_{-0.16}$	
χ^2/dof		57.5/53	59.9/62	

Notes. ^{u}unconstrained; ^{f}fixed. Model M: MYTORUS coupled component (Murphy & Yaqoob 2009) used for the circumnuclear absorber/reflector. Model T: TORUS component (Brightman & Nandra 2011) used for the circumnuclear absorber/reflector.

The presence of multiple hot gas components is common in many systems, especially starbursts (e.g., Konami et al. 2011; Mineo et al. 2012). However, the power of these components is very large in Mrk 34 and converting the soft band power to a star formation rate (SFR) using the $L_{0.5-2}$:SFR scaling relation from Mineo et al. (2012) implies a high SFR$_{\mathrm{X-ray}} > 140\ M_\odot$ yr^{-1} even when the scatter in the relation is accounted for.[32] One can compare this to the infrared-derived SFR$_{\mathrm{IR}}$ from the SFR:L_{8-1000} relation presented by Kennicutt (1998a). We find SFR$_{\mathrm{IR}} \approx 30(\pm 9)\ M_\odot$ yr^{-1}, which should be considered as an upper-limit because the AGN contribution to the infrared appears to be substantial. SFR$_{\mathrm{X-ray}}$ is much higher than SFR$_{\mathrm{IR}}$, suggesting that some other process may be powering the observed soft X-ray components.

Photoionization of circumnuclear gas is commonly observed in nearby AGNs (e.g., Guainazzi & Bianchi 2007) and is the most likely viable alternative. In the bright nearby galaxy NGC 4151, a photoionized X-ray component with similar fractional luminosity to hard X-rays as in Mrk 34 has been observed to spatially trace the extended [O III] emission (Wang et al. 2011). It may thus be the case that the entire soft X-ray regime in Mrk 34 is a complex of emission lines associated with extended photoionized gas in the narrow-line region. We attempted such a model by replacing the APEC components with several narrow emission features. A minimal set to give an acceptable fit included O VII Kα (0.571 keV), a narrow O VIII radiative recombination continuum (0.871 keV), and Ne X Kα (1.022 keV), with $\chi^2/\mathrm{dof} = 68.9/63$. The hard X-ray portion of the spectrum is still well fit in this case, but a much steeper scattered PL with $\Gamma = 2.7 \pm 0.2$ is required to fill in the gaps between the emission lines in the soft band. This indicates the need for extra emission lines, or possibly a weaker collisionally ionized component as has been observed in other AGNs (Guainazzi et al. 2009; Bianchi et al. 2010).

If photoionization dominates over scattering, this could explain the low $f_{\mathrm{scatt}} \lesssim 0.5\%$ (Table 2) associated with the intrinsic PL scattered into the line of sight by diffuse hot gas. Nearby Seyferts generally show f_{scatt} values of a few percent (e.g., Cappi et al. 2006). If part of this soft emission were instead attributed to X-ray binaries in the host galaxy, that would imply an even lower value of f_{scatt}. Alternative explanations could be a "buried AGN" with a geometrically thick torus (Ueda et al. 2007) or host galaxy extinction (Hönig et al. 2014), although neither obviously works for Mrk 34. The strong [O III] lines seen in this object are not typical of buried AGNs, and the small Balmer decrement (see Section 6.2) together with the intermediate inclination angle[33] of the galaxy disk of 45°, is consistent with only modest dust reddening in the host. Finally, another recent proposal on the origin of this soft emission component is scattering off clouds within a clumpy torus medium (Miniutti et al. 2014).

These issues can be investigated using higher spatial resolution imaging with *Chandra* and future high spectral resolution observations with *Astro-H* (Takahashi et al. 2012).

6.4. Comparison to Other Bona Fide CT AGNs

Figure 4 compares Mrk 34 on the $L_{2-10,\mathrm{in}}$ versus distance plane with all other bona fide CT AGNs from the compilation of Goulding et al. (2012), supplemented with recent results on individual sources, which have been collated in the Appendix. Some sources known to be of changing-look nature with rapid Compton-thick/thin transitions, such as NGC 1365 (Risaliti et al. 2005), have not been tabulated in this list in accordance with Della Ceca et al. (2008), though these are also potential candidates for inclusion. Note that Mrk 231 and NGC 7674 have been removed from this compilation based on results from Teng et al. (2014) and Bianchi et al. (2005). Recent *NuSTAR* observations of the former source show no evidence of CT columns, while the nature of obscuration in the latter is

---

[32] The relation by Mineo et al. (2012) actually assumes a MEKAL model instead of APEC, but there is no significant difference between these two in terms of the inferred luminosities for our data.

[33] http://leda.univ-lyon1.fr/
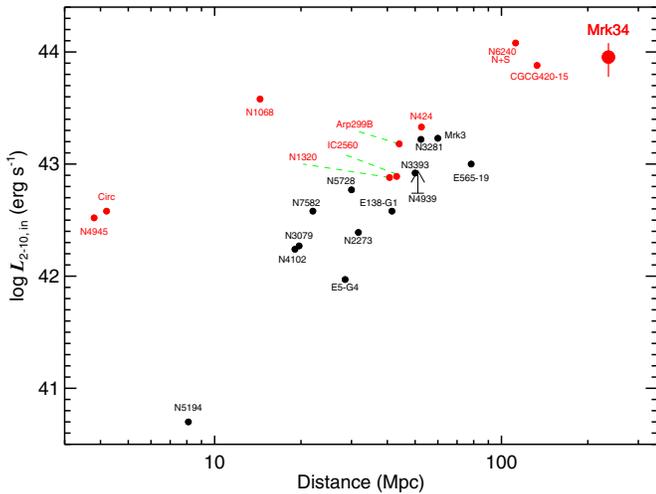
Figure 4. Intrinsic 2–10 keV luminosity vs. distance for the sample of bona fide CT AGNs from Goulding et al. (2012), updated and supplemented with other recent results. The data used to make this plot are collated in Table 3. Red denotes constraints from *NuSTAR*.

(A color version of this figure is available in the online journal.)

currently unclear with the source being either a changing-look AGN or having recently switched off. For another source, Superantennae, *NuSTAR* observations find a strong decrease in the broadband X-ray flux as compared to previous observations with *Suzaku*. Whether this is a result of dramatic luminosity decline, spectral change, or contaminating sources in previous data, is currently being investigated (S. H. Teng et al. 2014, in preparation), so this source is also currently not included in this compilation.

Mrk 34 emerges as one of the most luminous among the local bona fide CT AGNs, similar to NGC 6240. Given the extreme luminosities of these two sources within the local sample, it is interesting to compare and contrast their characteristics. For NGC 6240, we have reanalyzed the *BeppoSAX* data of Vignati et al. (1999) as well as new *NuSTAR* data and found a luminosity agreeing to within a factor of approximately two of the value of

$L_{2-10,in}$ quoted in Vignati et al. after correcting for cosmology and applying a correction factor for a toroidal obscuration geometry (S. Puccetti et al. 2014, in preparation). NGC 6240 appears to be somewhat less obscured and has a weaker Fe line than Mrk 34 ($N_H \approx 1 \times 10^{24}$ cm^{-2} and EW$_{K\alpha} \approx 0.3$ keV; Brightman & Nandra 2011).

NGC 6240 is a well-known binary AGN (Komossa et al. 2003) and its hard X-ray emission above 10 keV is the combined luminosity of both the northern (N) and the southern (S) components. The contribution of each component to the hard X-ray emission has not been directly resolved, but low-energy X-ray data, as well as mid-IR continuum imaging, show S to be brighter than N by a factor of a few (Komossa et al. 2003; Wang et al. 2014; Asmus et al. 2014). Mrk 34, on the other hand, is not a known binary AGN and is not in a major merger. Figure 5 presents *HST* images for the two objects, which makes the difference immediately clear. NGC 6240 has a total far-infrared power $L_{8-1000} \approx 6.5 \times 10^{11}$ $L_\odot$ (Sanders et al. 2003; Koss et al. 2013), which is about three times higher than that of Mrk 34. Both objects lie within the luminosity regime associated with LIRGs. We also note that the object that follows these two in terms of luminosity, CGCG 420-15 (Severgnini et al. 2011), has also been identified to lie in a group (Crook et al. 2007). In this case, we quote the intrinsic luminosity based upon our model fits to new *NuSTAR* data.

Is there any evidence for galaxy interaction in Mrk 34? The galaxy is classified morphologically as Hubble class Sa (Nair & Abraham 2010). From integral field spectroscopy, Stoklasová et al. (2009) found an asymmetry in the nuclear emission line distribution that is elongated at a position angle of 140°–150°. Twisted Hα velocity isocontours were also identified by them. However, these may be signatures of interaction between the AGN jet and narrow-line region clouds, as suggested by Falcke et al. (1998) based upon matching of radio and nar-rowband emission line maps. Any morphological perturbations related to galaxy interactions must then be relatively mild. Even if the present nuclear activity is a result of some past interaction or merger, Mrk 34 is clearly at a different evolutionary stage now as compared to the strongly interacting system NGC 6240.

Figure 5. Hubble Legacy Archive images of Mrk 34 and NGC 6240. The images are two-band color composites. For Mrk 34, WFPC2 images in filters F547M (red) and F467M (green) are combined; for NGC 6240, ACS filters used are F814W (red) and F435W (green). North is up and east is to the left in both panels. These images clearly show the relatively unperturbed disk morphology of Mrk 34 as compared to the strong ongoing interaction in NGC 6240.

(A color version of this figure is available in the online journal.)

Alternatively, these sources may be showcasing the contrast between the two dominant AGN-triggering modes—secular processes versus major mergers—with secular processes thought to dominate in the low-redshift universe (e.g., Draper & Ballantyne 2012).

In summary, Mrk 34 is not in a merging system at present, unlike NGC 6240. This makes Mrk 34 the closest known bona fide CT QSO in a non-merging system.

6.5. Feedback from the AGN?

At present, there is an absence of nuclear star formation in Mrk 34 (González Delgado et al. 2001; Stoklasová et al. 2009). Wang et al. (2007) classify Mrk 34 as undergoing suppressed star formation as a result of AGN feedback, with the present SFR surface density lying about two orders or magnitude lower than predicted by the Kennicutt–Schmidt Law (Kennicutt 1998b).

A spatially resolved ionized outflow with a maximum velocity of 1500 km s^{-1} and gas being accelerated out to a radius of 1 kpc has been observed in high angular resolution *HST* observations with the Space Telescope Imaging Spectrograph by Fischer et al. (2013). It is possible to estimate the potential impact of mechanical feedback associated with this ionized [O III] outflow. For this, we use the relation between $L_{\mathrm{[O III]}}$ (assuming that the line is fully associated with the outflow) and the kinetic power (P_K^{ion}) of this ionized component, as derived by Cano-Díaz et al. (2012). For typical electron densities of 10^{2-4} cm^{-3} expected in the narrow-line region, Equation (B.9) of Cano-Díaz et al. (2012) implies a kinetic power of $P_K^{\mathrm{ion}} \sim 4 \times 10^{41-43}$ erg s^{-1}. This constitutes ~0.05%–5% of the source (infrared) bolometric power, a typical level required by models for the outflow to have any significant impact on the host galaxy (e.g., Di Matteo et al. 2005; Hopkins & Elvis 2010).

As an alternative determination of the outflow power, we utilize the Hβ luminosity together with Equations (2) and (3) of Harrison et al. (2014). The line luminosity ($L_{\mathrm{H}\beta} = 2 \times 10^{41}$ erg s^{-1}) and width containing 80% of the flux ($W_{80} = 690$ km s^{-1}) were measured from the SDSS spectra as analyzed in Mullaney et al. (2013). In this case, the SDSS observations do not spatially resolve the line emission, thus we assume the extent and maximum speed of the Hβ line emitting material to be the same as that of the ionized gas (Fischer et al. 2013). These assumptions imply that the outflow has been constant for ≈1 Myr, which results in an ionized gas mass, $M_{\mathrm{gas}} \sim 6 \times 10^{5-7}\ M_\odot$, a kinetic energy, $E_{\mathrm{kin}} \sim 2 \times 10^{54-56}$ erg, and kinetic power, $\dot{E}_{\mathrm{kin}} \sim 4 \times 10^{40-42}$ erg s^{-1}, a range that is about one order of magnitude lower than the determination based on Cano-Díaz et al. (2012).

The above estimates use observed line luminosities, and a correction for reddening would push the corresponding power higher by a factor of a few. On the other hand, we assume that the line radiating ionized gas fully participates in the outflow, which is unlikely to be the case. For example, in the outflow estimates based upon Hβ, we incorporate the total observed narrow line flux rather than the clearly outflowing (blueshifted) components. These estimates would then provide upper limits on the outflow, though spherical and wide-angle outflows with small velocity differences across them have been observed in many systems (e.g., Liu et al. 2013; Harrison et al. 2014). Therefore, mechanical feedback may have a significant effect in Mrk 34; however, there are plenty of uncertainties in the present estimates.
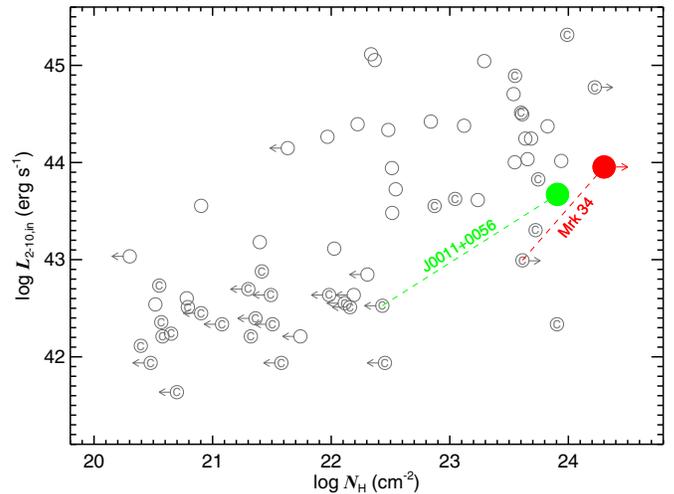
Figure 6. N_{H} vs. $L_{2-10,\,\mathrm{in}}$ for all X-ray-detected SDSS QSO2s (gray), based only on direct continuum modeling of X-ray data below 10 keV, collated from Vignali et al. (2006, 2010), Jia et al. (2013), and LaMassa et al. (2014). N_{H} upper limits are denoted by arrows and CT candidates are denoted with "C." Recall that CT candidacy is often based on indirect multiwavelength indicators, and direct continuum fitting to low-energy X-ray data of faint, obscured AGNs is very inefficient at securely identifying CT sources. This is why many CT candidates have apparent $N_{\mathrm{H}} \ll 10^{24}$ cm^{-2} at present, and their plotted values of $L_{2-10,\,\mathrm{in}}$ are also likely to be underestimates. The large filled points are the updated values from *NuSTAR* modeling for the two *NuSTAR*-detected sources (Mrk 34 in red and SDSS J0011+0056 in green, respectively, where the latter is reported in Lansbury et al. 2014).

(A color version of this figure is available in the online journal.)

In any case, the presence of CT gas columns as inferred from the *NuSTAR* data means that such feedback has not yet removed the nuclear obscuring gas. Any jet-induced interaction is expected to have most impact along the jet axis. The source has a bipolar radio morphology and shows two hot spots (Falcke et al. 1998), thus the jet is pointed out of our line of sight and would not directly impact the toroidal obscuring gas. Direct radiation pressure is also unlikely to be effective in removing obscuring gas when the column density becomes CT (e.g., Fabian et al. 2008). However, radiation pressure could be the physical driver of the ionized outflow.

6.6. Implications for Distant Obscured AGN Studies

Figure 6 shows our present constraints on N_{H} and the intrinsic $L_{\mathrm{X\text{-}ray}}$ for the X-ray-detected SDSS-QSO2 population. In gray are the measurements for all 63 sources detected by *Chandra*/ *XMM-Newton* and with an N_{H} measurement based upon X-ray spectral fitting with data below 10 keV, collated from Vignali et al. (2006, 2010), Jia et al. (2013) and LaMassa et al. (2014). For sources with multiple fits (either to data from multiple observations or from using multiple models), we chose fits based on recent physically motivated torus models when available, otherwise preferring the highest fitted N_{H} values. In red and green are the new constraints from the broadband modeling of the two *NuSTAR*-detected QSO2s Mrk 34 and SDSS J0011+0056, respectively. Direct continuum modeling of data below 10 keV underestimates N_{H} and intrinsic $L_{\mathrm{X\text{-}ray}}$ for both, and the improved constraints enabled by *NuSTAR* move both quantities to significantly higher values. Therefore, the plotted values of N_{H} and $L_{2-10,\,\mathrm{in}}$ may actually be *underestimates* for other sources as well, especially the CT candidates. If this trend turns out to hold for many of these candidates, this will have important implications for AGN population models,

which require a good knowledge of the underlying column density and luminosity distributions. Observations of more QSO2s with *NuSTAR* would be invaluable for obtaining improved constraints on the overall population.

Studies of distant obscured AGNs are extremely challenging even with *NuSTAR*, as is evident from the non-detection of all sources except one in two recent exploratory *NuSTAR* studies targeting luminous QSO2s at $z \sim 0.5$ (Lansbury et al. 2014) and hyperluminous infrared galaxies at $z \sim 2$ (Stern et al. 2014), respectively. Mrk 34 is the first source in a similar class to show enough photons for X-ray spectral modeling. Its brightness is a result of its lower redshift as compared to the previously targeted sources. This, together with the fact that Mrk 34 appears to be a typical CT QSO (as discussed before), means that the X-ray spectrum of Mrk 34 can serve as a useful template for more distant CT QSOs. In particular, Mrk 34 is a factor of two to three more luminous than NGC 1068, and shows evidence of a higher level of obscuration as compared to NGC 6240 (see Section 6.4), the two other sources often considered as CT AGN archetypes.

An important point is that Mrk 34 would not have been *selected* as an obscured quasar from modeling of the X-ray continuum below 10 keV alone, because absorption correction of the *XMM-Newton* data without higher energy coverage results in intrinsic luminosities that are $\gtrsim 10$ times lower than found by *NuSTAR* (Section 2). This means that X-ray selection of obscured quasars from data with low spectral statistics can severely underestimate N_H as well as the intrinsic X-ray power, leading to biased estimates of the distributions of these quantities. While the high $EW_{K\alpha}$ in Mrk 34 was known previously and gave a strong hint supporting CT obscuration, the detection and identification of this narrow feature require a reasonable count rate, which is not available for most AGNs found in typical distant X-ray surveys. Expanded deep surveys with *Chandra* and *XMM-Newton* (e.g., the upcoming 7 Ms Chandra Deep Field South) will help in this regard, as will detailed follow-up with future missions such as *Astro-H* and *Athena* (Takahashi et al. 2012; Nandra et al. 2013).

7. SUMMARY

Combining *NuSTAR* observations with archival *XMM-Newton* data, we have carried out high-quality broadband X-ray spectroscopy of the optically selected QSO2 Mrk 34. A summary of our main results is as follows.

1. Using two physically motivated toroidal obscuration models, we show that the spectra are fully consistent with obscuration by CT column densities of gas along the line of sight. This is the first time that such high columns have been directly measured from spectral fitting to the X-ray continuum of an SDSS-QSO2. This has been possible thanks to the hard X-ray sensitivity of *NuSTAR*.

2. Comparisons of the intrinsic luminosity inferred from the two torus models with various multiwavelength luminosity correlations suggest that our X-ray analysis reliably measures the intrinsic source power of $L_{2-10,in} \sim 10^{44}$ erg s^{-1} to within a factor of ~ 2. When converted to a bolometric luminosity, the accretion power is sufficient to drive the entire infrared emission.

3. The observed soft X-ray emission appears to be too luminous to be associated with star formation and may instead be driven by AGN photoionization.

4. Mrk 34 is representative of the SDSS-QSO2 population in terms of its [O III] line luminosity, and it shows all the indirect pieces of evidence expected for sources with CT obscuration (i.e., a low observed X-ray luminosity with respect to other isotropic AGN luminosity indicators, a powerful H$_2$O megamaser, and a strong Fe Kα line). Thus, Mrk 34 is a benchmark CT QSO2 in the local universe. It is the nearest isolated CT quasar in that it is not presently undergoing a major merger.

5. However, using X-ray data below 10 keV alone fails to pick up the source as an intrinsically luminous AGN. This has implications for low-energy X-ray selection of obscured quasars in survey fields where most detected sources lie in the low-count regime, and more *NuSTAR* observations of CT QSO2 candidates are required for understanding the importance of this selection effect. Our broadband X-ray spectrum of Mrk 34 could serve as a useful local template for hard X-ray studies of distant CT quasars.

APPENDIX

LIST OF BONA FIDE LOCAL COMPTON-THICK AGNs

Table 3 lists the distances and intrinsic luminosities of all the bona fide CT AGNs plotted in Figure 4, along with relevant references for their X-ray analyses.

Table 3
List of Bona Fide Local Compton-thick AGNs

Source	Distance (Mpc)	$L_{2-10,in}$ (erg s^{-1})	Reference
NGC 424	52.6	43.33	1
NGC 1068	14.4	43.58	2
NGC 1320	40.7	42.88	1
CGCG420-15	133.0	43.88	3, 4
ESO 005-G004	28.5	41.97	
Mrk 3	60.0	43.23	5
NGC 2273	31.7	42.39	
ESO 565-G019	78.4	43.00	6
NGC 3079	19.7	42.27	
IC 2560	43.1	42.89	1
NGC 3281	52.4	43.22	
Mrk 34	236.0	43.95	4
NGC 3393	50.0	42.92	7
Arp 299B	44.0	43.18	8
NGC 4102	19.0	42.24	9
NGC 4939	51.1	42.74	
NGC 4945	3.8	42.52	10
NGC 5194	8.1	40.70	
Circinus	4.2	42.58	11
NGC 5728	30.0	42.77	
ESO 138-G001	41.5	42.58	
NGC 6240	112.0	44.08	12, 13
NGC 7582	22.0	42.58	

Notes. Distances are redshift-independent estimates from NED for the closest sources, or luminosity distances from the respective references, which were corrected for cosmology.
References. (1) Baloković et al. 2014; (2) F. E. Bauer et al. 2014 (in preparation); (3) Severgnini et al. 2011; (4) this work; (5) Awaki et al. 2008; (6) Gandhi et al. 2013; (7) Fabbiano et al. 2011; (8) Ptak et al. 2014; (9) González-Martín et al. 2011; (10) Puccetti et al. 2014; (11) Arévalo et al. 2014; (12) Vignati et al. 1999; (13) S. Puccetti et al. 2014 (in preparation). Where not stated, the reference is the compilation by Goulding et al. (2012) and papers referred to therein. Mrk 231, NGC 7674, and IRAS 19254-72 are not included as a result of recent updates to the intrinsic luminosities (see the text).

REFERENCES

Akylas, A., Georgakakis, A., Georgantopoulos, I., Brightman, M., & Nandra, K. 2012, A&A, 546, A98
Alexander, D. M., Stern, D., Del Moro, A., et al. 2013, ApJ, 773, 125
Alonso-Herrero, A., Pereira-Santaella, M., Rieke, G. H., & Rigopoulou, D. 2012, ApJ, 744, 2
Arévalo, P., Bauer, F. E., Puccetti, S., et al. 2014, ApJ, 791, 81
Arnaud, K. A. 1996, in ASP Conf. Ser. 101, Astronomical Data Analysis Software and Systems V, ed. G. H. Jacoby & J. Barnes (San Francisco, CA: ASP), 17
Asmus, D., Gandhi, P., Smette, A., Hönig, S. F., & Duschl, W. J. 2011, A&A, 536, A36
Asmus, D., Hönig, S. F., Gandhi, P., Smette, A., & Duschl, W. J. 2014, MNRAS, 439, 1648
Assef, R. J., Stern, D., Kochanek, C. S., et al. 2013, ApJ, 772, 26
Awaki, H., Anabuki, N., Fukazawa, Y., et al. 2008, PASJ, 60, 293
Ballantyne, D. R., Draper, A. R., Madsen, K. K., Rigby, J. R., & Treister, E. 2011, ApJ, 736, 56
Baloković, M., Comastri, A., Harrison, F., et al. 2014, ApJ, in press
Bassani, L., Dadina, M., Maiolino, R., et al. 1999, ApJS, 121, 473
Baumgartner, W. H., Tueller, J., Markwardt, C. B., et al. 2013, ApJS, 207, 19
Bianchi, S., Chiaberge, M., Evans, D. A., et al. 2010, MNRAS, 405, 553
Bianchi, S., Guainazzi, M., Matt, G., et al. 2005, A&A, 442, 185
Bolton, A. S., Schlegel, D. J., Aubourg, É., et al. 2012, AJ, 144, 144
Boroson, T. A., & Green, R. F. 1992, ApJS, 80, 109
Brightman, M., & Nandra, K. 2011, MNRAS, 413, 1206
Brightman, M., & Ueda, Y. 2012, MNRAS, 423, 702
Burlon, D., Ajello, M., Greiner, J., et al. 2011, ApJ, 728, 58

Cano-Díaz, M., Maiolino, R., Marconi, A., et al. 2012, A&A, 537, L8
Cappi, M., Panessa, F., Bassani, L., et al. 2006, A&A, 446, 459
Comastri, A., Ranalli, P., Iwasawa, K., et al. 2011, A&A, 526, L9
Comastri, A., Setti, G., Zamorani, G., & Hasinger, G. 1995, A&A, 296, 1
Crook, A. C., Huchra, J. P., Martimbeau, N., et al. 2007, ApJ, 655, 790
Dahari, O., & De Robertis, M. M. 1988, ApJS, 67, 249
Del Moro, A., Mullaney, J. R., Alexander, D. M., et al. 2014, ApJ, 786, 16
Della Ceca, R., Severgnini, P., Caccianiga, A., et al. 2008, MmSAI, 79, 65
Di Matteo, T., Springel, V., & Hernquist, L. 2005, Natur, 433, 604
Dickey, J. M., & Lockman, F. J. 1990, ARA&A, 28, 215
Done, C., Madejski, G. M., Życki, P. T., & Greenhill, L. J. 2003, ApJ, 588, 763
Donley, J. L., Koekemoer, A. M., Brusa, M., et al. 2012, ApJ, 748, 142
Draper, A. R., & Ballantyne, D. R. 2010, ApJL, 715, L99
Draper, A. R., & Ballantyne, D. R. 2012, ApJ, 751, 72
Elvis, M., Wilkes, B. J., McDowell, J. C., et al. 1994, ApJS, 95, 1
Fabbiano, G., Wang, J., Elvis, M., & Risaliti, G. 2011, Natur, 477, 431
Fabian, A. C., Vasudevan, R. V., & Gandhi, P. 2008, MNRAS, 385, L43
Falcke, H., Wilson, A. S., & Simpson, C. 1998, ApJ, 502, 199
Feruglio, C., Daddi, E., Fiore, F., et al. 2011, ApJL, 729, L4
Fischer, T. C., Crenshaw, D. M., Kraemer, S. B., & Schmitt, H. R. 2013, ApJS, 209, 1
Gandhi, P., Crawford, C. S., Fabian, A. C., & Johnstone, R. M. 2004, MNRAS, 348, 529
Gandhi, P., & Fabian, A. C. 2003, MNRAS, 339, 1095
Gandhi, P., Fabian, A. C., & Crawford, C. S. 2006, MNRAS, 369, 1566
Gandhi, P., Fabian, A. C., Suebsuwong, T., et al. 2007, MNRAS, 382, 1005
Gandhi, P., Horst, H., Smette, A., et al. 2009, A&A, 502, 457
Gandhi, P., Terashima, Y., Yamada, S., et al. 2013, ApJ, 773, 51
Georgantopoulos, I., Comastri, A., Vignali, C., et al. 2013, A&A, 555, A43
Gilli, R., Comastri, A., & Hasinger, G. 2007, A&A, 463, 79
González Delgado, R. M., Heckman, T., & Leitherer, C. 2001, ApJ, 546, 845
González-Martín, O., Papadakis, I., Braito, V., et al. 2011, A&A, 527, A142
Goulding, A. D., Alexander, D. M., Bauer, F. E., et al. 2012, ApJ, 755, 5
Greenhill, L. J., Tilak, A., & Madejski, G. 2008, ApJL, 686, L13
Guainazzi, M., & Bianchi, S. 2007, MNRAS, 374, 1290
Guainazzi, M., Risaliti, G., Nucita, A., et al. 2009, A&A, 505, 589
Harrison, C. M., Alexander, D. M., Mullaney, J. R., & Swinbank, A. M. 2014, MNRAS, 441, 3306
Harrison, F. A., Craig, W. W., Christensen, F. E., et al. 2013, ApJ, 770, 103
Heckman, T. M., Miley, G. K., van Breugel, W. J. M., & Butcher, H. R. 1981, ApJ, 247, 403
Henkel, C., Peck, A. B., Tarchi, A., et al. 2005, A&A, 436, 75
Hickox, R. C., Mullaney, J. R., Alexander, D. M., et al. 2014, ApJ, 782, 9
Hönig, S. F., Gandhi, P., Asmus, D., et al. 2014, MNRAS, 438, 647
Hopkins, P. F., & Elvis, M. 2010, MNRAS, 401, 7
Jia, J., Ptak, A., Heckman, T., & Zakamska, N. L. 2013, ApJ, 777, 27
Kennicutt, R. C., Jr. 1998a, ARA&A, 36, 189
Kennicutt, R. C., Jr. 1998b, ApJ, 498, 541
Kirsch, M. G. F., Altieri, B., Chen, B., et al. 2004, Proc. SPIE, 5488, 103
Komossa, S., Burwitz, V., Hasinger, G., et al. 2003, ApJL, 582, L15
Konami, S., Matsushita, K., Tsuru, T. G., Gandhi, P., & Tamagawa, T. 2011, PASJ, 63, 913
Kondratko, P. T., Greenhill, L. J., & Moran, J. M. 2006, ApJ, 652, 136
Koss, M., Mushotzky, R., Baumgartner, W., et al. 2013, ApJL, 765, L26
Kuo, C. Y., Braatz, J. A., Condon, J. J., et al. 2011, ApJ, 727, 20
Lacy, M., Storrie-Lombardi, L. J., Sajina, A., et al. 2004, ApJS, 154, 166
LaMassa, S. M., Yaqoob, T., Ptak, A. F., et al. 2014, ApJ, 787, 61
Lansbury, G. B., Alexander, D. M., Del Moro, A., et al. 2014, ApJ, 785, 17
Liu, G., Zakamska, N. L., Greene, J. E., Nesvadba, N. P. H., & Liu, X. 2013, MNRAS, 436, 2576
Magdziarz, P., & Zdziarski, A. A. 1995, MNRAS, 273, 837
Mainieri, V., Bongiorno, A., Merloni, A., et al. 2011, A&A, 535, A80
Marconi, A., & Hunt, L. K. 2003, ApJL, 589, L21
Mateos, S. 2005, A&A, 433, 855
Mateos, S., Alonso-Herrero, A., Carrera, F. J., et al. 2012, MNRAS, 426, 3271
Matt, G., Fabian, A. C., Guainazzi, M., et al. 2000, MNRAS, 318, 173
McCarthy, P. J. 1993, ARA&A, 31, 639
McConnell, N. J., & Ma, C.-P. 2013, ApJ, 764, 184
Merloni, A., Bongiorno, A., Brusa, M., et al. 2014, MNRAS, 437, 3550
Miley, G., & De Breuck, C. 2008, A&ARv, 15, 67
Mineo, S., Gilfanov, M., & Sunyaev, R. 2012, MNRAS, 426, 1870
Miniutti, G., Sanfrutos, M., Beuchert, T., et al. 2014, MNRAS, 437, 1776
Mulchaey, J. S., Koratkar, A., Ward, M. J., et al. 1994, ApJ, 436, 586
Mullaney, J. R., Alexander, D. M., Fine, S., et al. 2013, MNRAS, 433, 622
Murphy, K. D., & Yaqoob, T. 2009, MNRAS, 397, 1549
Nair, P. B., & Abraham, R. G. 2010, ApJS, 186, 427

Nandra, K., Barret, D., Barcons, X., et al. 2013, The Hot and Energetic Universe: A White Paper Presenting the Science Theme Motivating the Athena+ Mission (arXiv:1306.2307)

Nandra, K., George, I. M., Mushotzky, R. F., Turner, T. J., & Yaqoob, T. 1997, ApJL, 488, L91

Nandra, K., O'Neill, P. M., George, I. M., & Reeves, J. N. 2007, MNRAS, 382, 194

Netzer, H., Mainieri, V., Rosati, P., & Trakhtenbrot, B. 2006, A&A, 453, 525

Norman, C., Hasinger, G., Giacconi, R., et al. 2002, ApJ, 571, 218

Oh, K., Sarzi, M., Schawinski, K., & Yi, S. K. 2011, ApJS, 195, 13

Panessa, F., Bassani, L., Cappi, M., et al. 2006, A&A, 455, 173

Pfefferkorn, F., Boller, T., & Rafanelli, P. 2001, A&A, 368, 797

Piconcelli, E., Jimenez-Bailón, E., Guainazzi, M., et al. 2005, A&A, 432, 15

Planck, Collaboration, Ade, P. A. R., Aghanim, N., et al. 2013, A&A, in press (arXiv:1303.5076)

Ptak, A., Zakamska, N. L., Strauss, M. A., et al. 2006, ApJ, 637, 147

Ptak, A., Hornschemeier, A., Zezas, A., et al. 2014, ApJ, submitted

Puccetti, S., Comastri, A., Fiore, F., et al. 2014, ApJ, in press (arXiv:1407.3974)

Reyes, R., Zakamska, N. L., Strauss, M. A., et al. 2008, AJ, 136, 2373

Ricci, C., Walter, R., Courvoisier, T. J.-L., & Paltani, S. 2011, A&A, 532, A102

Risaliti, G., Elvis, M., Fabbiano, G., Baldi, A., & Zezas, A. 2005, ApJL, 623, L93

Sanders, D. B., Mazzarella, J. M., Kim, D.-C., Surace, J. A., & Soifer, B. T. 2003, AJ, 126, 1607

Schlafly, E. F., & Finkbeiner, D. P. 2011, ApJ, 737, 103

Severgnini, P., Caccianiga, A., Della Ceca, R., et al. 2011, A&A, 525, A38

Smith, R. K., Brickhouse, N. S., Liedahl, D. A., & Raymond, J. C. 2001, ApJL, 556, L91

Stern, D., Assef, R. J., Benford, D. J., et al. 2012, ApJ, 753, 30

Stern, D., Eisenhardt, P., Gorjian, V., et al. 2005, ApJ, 631, 163

Stern, D., Lansbury, G. B., Assef, R. J., et al. 2014, ApJ, in press (arXiv:1403.3078)

Stern, D., Moran, E. C., Coil, A. L., et al. 2002, ApJ, 568, 71

Stoklasová, I., Ferruit, P., Emsellem, E., et al. 2009, A&A, 500, 1287

Takahashi, T., Mitsuda, K., Kelley, R., et al. 2012, Proc. SPIE, 8443, 84431Z

Teng, S. H., Brandt, W. N., Harrison, F. A., et al. 2014, ApJ, 785, 19

Tozzi, P., Mainieri, V., Rosati, P., et al. 2009, ApJ, 698, 740

Treister, E., Urry, C. M., & Virani, S. 2009, ApJ, 696, 110

Tremaine, S., Gebhardt, K., Bender, R., et al. 2002, ApJ, 574, 740

Ueda, Y., Akiyama, M., Hasinger, G., Miyaji, T., & Watson, M. G. 2014, ApJ, 786, 104

Ueda, Y., Eguchi, S., Terashima, Y., et al. 2007, ApJL, 664, L79

Ulvestad, J. S., & Wilson, A. S. 1984, ApJ, 278, 544

Vasudevan, R. V., Fabian, A. C., Gandhi, P., Winter, L. M., & Mushotzky, R. F. 2010, MNRAS, 402, 1081

Vasudevan, R. V., Mushotzky, R. F., & Gandhi, P. 2013, ApJL, 770, L37

Veilleux, S., Rupke, D. S. N., Kim, D.-C., et al. 2009, ApJS, 182, 628

Vignali, C., Alexander, D. M., & Comastri, A. 2004, MNRAS, 354, 720

Vignali, C., Alexander, D. M., & Comastri, A. 2006, MNRAS, 373, 321

Vignali, C., Alexander, D. M., Gilli, R., & Pozzi, F. 2010, MNRAS, 404, 48

Vignati, P., Molendi, S., Matt, G., et al. 1999, A&A, 349, L57

Wang, J., Fabbiano, G., Elvis, M., et al. 2011, ApJ, 742, 23

Wang, J., Nardini, E., Fabbiano, G., et al. 2014, ApJ, 781, 55

Wang, J.-M., Chen, Y.-M., Yan, C.-S., Hu, C., & Bian, W.-H. 2007, ApJL, 661, L143

Wilkes, B. J., Kuraszkiewicz, J., Haas, M., et al. 2013, ApJ, 773, 15

Wright, E. L., Eisenhardt, P. R. M., Mainzer, A. K., et al. 2010, AJ, 140, 1868

Yaqoob, T. 2012, MNRAS, 423, 3360

Zakamska, N. L., Strauss, M. A., Krolik, J. H., et al. 2003, AJ, 126, 2125